nature geoscience

ARTICLES

https://doi.org/10.1038/s41561-018-0207-4

West Antarctic Ice Sheet retreat in the Amundsen Sea driven by decadal oceanic variability

Adrian Jenkins[1*], Deb Shoosmith[1], Pierre Dutrieux[2], Stan Jacobs[2], Tae Wan Kim[3], Sang Hoon Lee[3], Ho Kyung Ha[4] and Sharon Stammerjohn[5]

Mass loss from the Amundsen Sea sector of the West Antarctic Ice Sheet has increased in recent decades, suggestive of sustained ocean forcing or an ongoing, possibly unstable, response to a past climate anomaly. Lengthening satellite records appear to be incompatible with either process, however, revealing both periodic hiatuses in acceleration and intermittent episodes of thinning. Here we use ocean temperature, salinity, dissolved-oxygen and current measurements taken from 2000 to 2016 near the Dotson Ice Shelf to determine temporal changes in net basal melting. A decadal cycle dominates the ocean record, with melt changing by a factor of about four between cool and warm extremes via a nonlinear relationship with ocean temperature. A warm phase that peaked around 2009 coincided with ice-shelf thinning and retreat of the grounding line, which re-advanced during a post-2011 cool phase. These observations demonstrate how discontinuous ice retreat is linked with ocean variability, and that the strength and timing of decadal extremes is more influential than changes in the longer-term mean state. The nonlinear response of melting to temperature change heightens the sensitivity of Amundsen Sea ice shelves to such variability, possibly explaining the vulnerability of the ice sheet in that sector, where subsurface ocean temperatures are relatively high.

The West Antarctic Ice Sheet (WAIS) has recently been contributing about 0.3 mm yr^{-1} to global sea level rise[1], with the potential to discharge ice more rapidly into the ocean where its bed slopes downward inland to as much as 2.5 km below sea level at its centre[2]. That configuration can be inherently unstable[3] unless floating ice shelves at its margin provide sufficient restraint on ice discharge across the grounding line[4,5]. Since buttressing is generated where ice shelves contact lateral margins and seabed shoals, ice-shelf thinning reduces buttressing, accelerating the outflow of grounded ice[6], a process that makes the WAIS highly sensitive to ocean conditions at its margin. Understanding the physical links between oceanic change and ice loss is thus critical to assessing the future of WAIS, and the potential reversibility of recent changes.

Satellite observations provide a consistent picture of mass loss from West Antarctica's Amundsen Sea sector over recent decades[1,7–9]. Flow acceleration of outlet glaciers[7] has been accompanied by inland thinning[1,9] and retreat of grounding lines[8], while lengthening records have revealed elevated rates of mass loss in recent years[1,7]. Key outlet glaciers are buttressed only by small ice shelves[10] that are furthermore exposed to relatively warm seawater[11]. The thinning signature propagates inland from grounding lines[9], with downstream ice shelves thinning faster[12], pointing to changes in buttressing triggered by ocean-driven melting as the cause.

Most studies have attributed the mass loss either to unstable retreat of the grounding lines[13,14], possibly triggered by a climate anomaly in the 1940s[15], or to sustained ocean forcing resulting from a past increase in the quantity of warm water on the continental shelf[16] or a long-term warming of those waters[17]. Recent observations[7–9] are, however, irreconcilable with such hypotheses. Alternating phases of rapid acceleration and steady or even decelerating flow are mostly coherent across different glaciers[7]. If all were retreating unstably or under sustained forcing, variations in the rate of change would be dictated by the geometry and flow regime of individual glaciers, and incoherent. Furthermore, current episodes of rapid thinning commenced on Pine Island and Thwaites glaciers less than 30 years ago[9], excluding a simple link with events in the 1940s.

Oceanographic records remain short and patchy on the Amundsen Sea continental shelf, where the first full-depth profiles of seawater properties in the early 1990s revealed warm derivatives of Circumpolar Deep Water in deep, glacially scoured troughs and a consequent high melt rate beneath Pine Island Ice Shelf[11]. Subsequent summer cruises indicated that Pine Island melt rates tracked ocean heat content, increasing between 1994 and 2009[18] and decreasing between 2010 and 2012[19]. The cool phase persisted for several years[20], causing deceleration of the glacier that has typically been interpreted as a minor perturbation to the long-term retreat[21,22]. Getz Ice Shelf experienced a more pronounced change in melting between cool ocean conditions in 2000 and warm in 2007[23], but the inland ice response remains undocumented. For both ice shelves, ship-based measurements have been limited by persistent sea ice fields, but near-repeat stations throughout the Amundsen continental shelf indicate spatially coherent cool and warm periods[24].

Melt rates inferred from observation at Dotson Ice Front

In this region, the most reliable area of summer open water is the Amundsen Sea polynya, which forms to the north of the Dotson and eastern Getz ice shelves. Ships have thus been able to access that area more often, yielding eight near-repeat sets of seawater properties close to the Dotson Ice Front from 2000 to 2016 (Fig. 1). Combining those observations shows how Dotson basal melting has evolved in response to changing ocean conditions.

The ice-front water column comprises two relatively uniform layers separated by a region with higher vertical thermohaline gradients (Fig. 2). The warmer and saltier bottom layer (typically near 0.5 °C and 34.55), is derived from modified Circumpolar Deep

[1]British Antarctic Survey, Natural Environment Research Council, Cambridge, UK. [2]Lamont-Doherty Earth Observatory of Columbia University, Palisades, NY, USA. [3]Korea Polar Research Institute, Incheon, Korea. [4]Department of Ocean Sciences, Inha University, Incheon, Korea. [5]Institute of Arctic and Alpine Research, University of Colorado, Boulder, CO, USA. *e-mail: ajen@bas.ac.uk

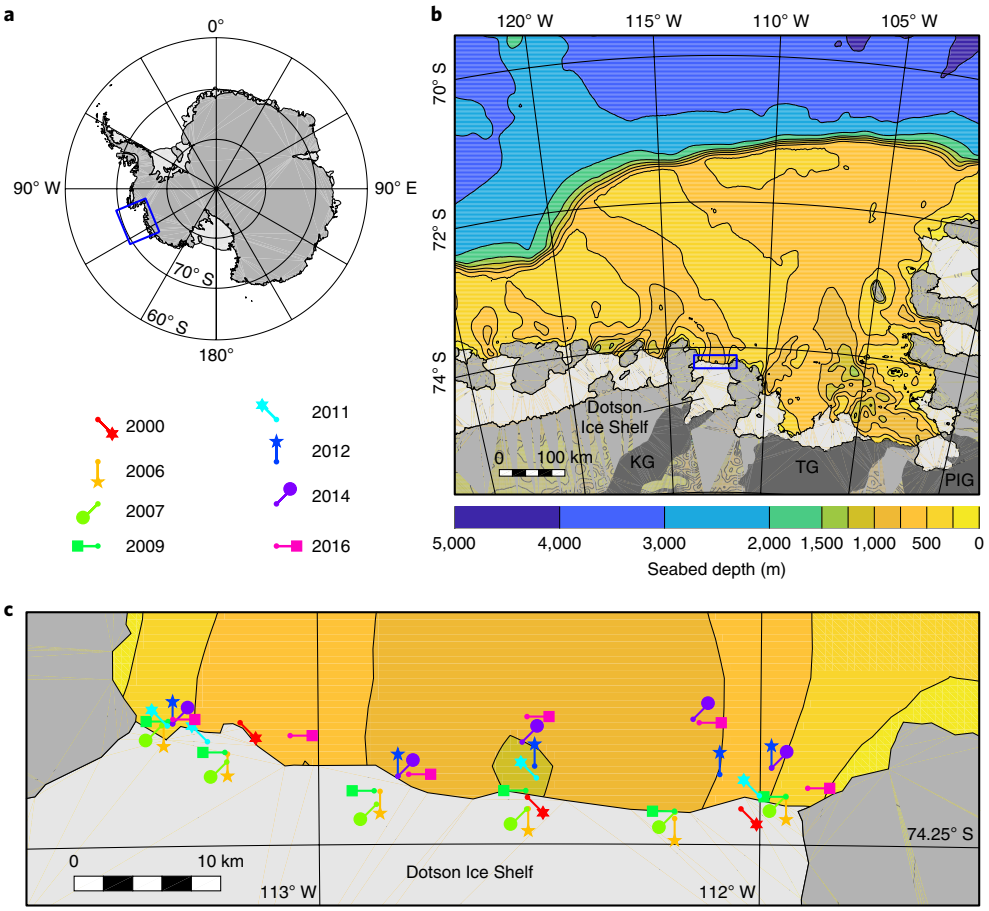

Fig. 1 | Locations of Amundsen Sea observations used in this study. a, Map of Antarctica indicating grounded ice sheet (darker shading), floating ice shelves (lighter shading) and study area (blue box). **b**, Enlargement of study area showing regional bathymetry[2] and catchments (darker shading) of Kohler, Thwaites and Pine Island glaciers (KG, TG, PIG). **c**, Enlargement of area near the moving Dotson Ice Front (blue box in panel **b**) showing locations and the years of summer (Dec–Mar) vertical profiles of seawater properties.

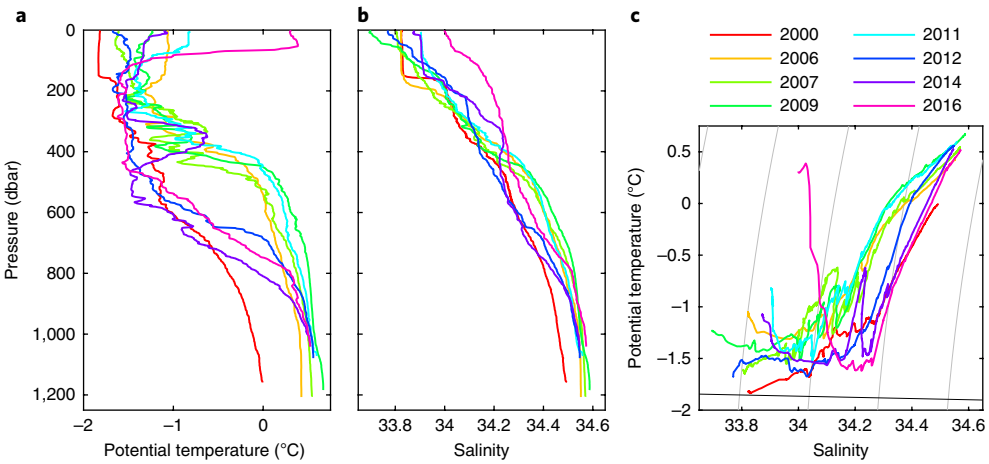

Fig. 2 | Potential temperature and salinity at Dotson Ice Front. a, Vertical profiles of potential temperature recorded at the deepest station sampled in each summer; centrally located in the trough near 112.5° W (Fig. 1c). **b**, Vertical profiles of salinity recorded at the same stations. **c**, Potential temperature versus salinity for the stations in panels **a** and **b**. Grey lines connect points of equal potential density (1,027–1,027.8 kg m^{-3} in 0.2 kg m^{-3} increments), while the black line indicates the surface freezing point.

Water (mCDW) that flows onto the shelf near 118° W and circulates cyclonically within the Dotson–Getz Trough[25,26]. The colder, fresher upper layer (typically near −1.25 °C and 33.8) is derived from Winter Water, formed as a result of cooling, brine drainage and convection beneath growing sea ice, and having properties that vary mainly through the degree of summer warming and the depth of winter mixing. The bottom layer was coldest in 2000, but more striking temperature changes occur near the mid-depth transition

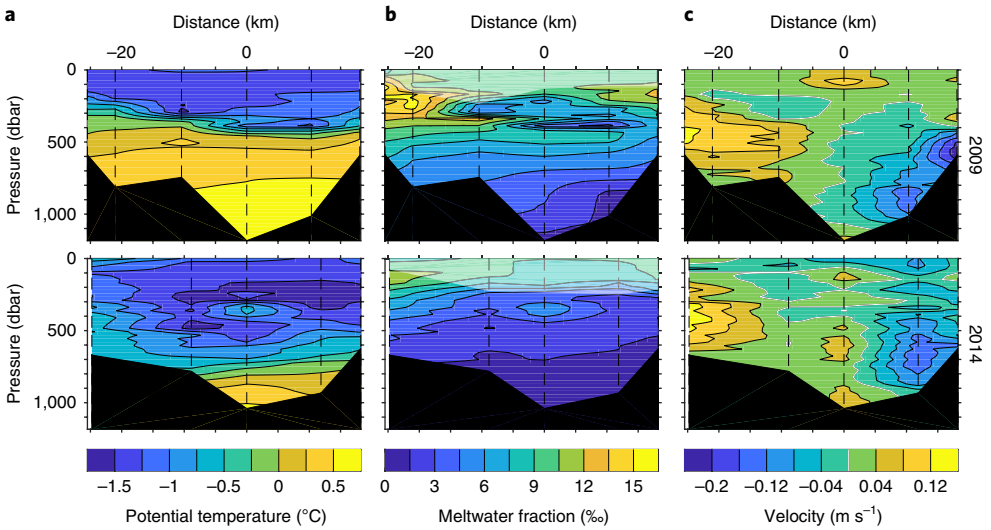

Fig. 3 | Cross-sections of potential temperature, meltwater fraction and current speed perpendicular to the ice front in different years. a, Potential temperature at stations (vertical dashed lines) in 2009 (top) and 2014 (bottom). Distance relative to the central trough station (Fig. 2) is positive eastward, and black shading shows the seabed, linearly interpolated between stations. **b**, Meltwater fraction derived from potential temperature, salinity and dissolved oxygen concentration (Methods); colours are lighter where the calculation is unreliable owing to the influence of air–sea interactions. **c**, Lowered Acoustic Doppler Current Profiler speeds perpendicular to the ice front, positive for northward outflows.

region between the two layers (Fig. 2). When that thermocline is shallow (deep), significantly more (less) ocean heat is available to melt ice within the sub-Dotson cavity. Deep thermoclines in 2000 and 2012–2016 bracket shallower levels in 2006–2011, changes that are coherent with less complete records elsewhere[18,19,23], albeit with systematic spatial differences[24].

After calculating seawater density from temperature and salinity, those parameters are used to determine the circulation and transport of meltwater across the ice front (Methods). In years when ocean current profiles were directly measured, their combination with seawater properties yields independent estimates of circulation and melting. A persistent east-side inflow that is warmer and deeper than the west-side outflow is consistent with the addition of meltwater from the ice-shelf base driving a geostrophic circulation (Fig. 3). More variable transports appear elsewhere across the section.

Estimates of the net meltwater flux across the sections closely track variations in mean temperature above freezing associated with changes in thermocline depth (Fig. 4a). Both quantities are estimated using observations over the entire section, but exclude a variable-depth surface layer where air-sea interaction influences the water properties (Methods). Meltwater fluxes were about four times higher at the peak warm phase in 2009 than during cool phases before and after, when values were similar despite the change in deep temperature maximum (Fig. 2a). Intermediate melt rates in 2006 and 2007 are consistent with a glaciological estimate[27] derived from 2003–2008 satellite data (Fig. 4a). Satellite-based estimates of spatial[28] and temporal[29,30] variability in Dotson Ice Shelf melting combine ice thicknesses derived from surface elevation data (a procedure that magnifies uncertainties by an order of magnitude) with surface accumulation and firn compaction rates both either derived from models that lack independent verification[29] or assumed constant[30]. Although subject to their own methodological uncertainty, our estimates are independent of regional climate models and assumptions about firn density.

Ice-sheet changes driven by melt rate variability

The 16-year history of melting explains the recently observed behaviour of Dotson Ice Shelf and its tributary ice streams, especially Kohler Glacier (Fig. 4b). Surface accumulation and iceberg calving make small, mutually cancelling contributions to the Dotson mass budget[27], so when melt equals ice flux across the grounding line the ice shelf is close to equilibrium. The low, near-equilibrium melt rate in 2000 was followed by four years of steady ice influx[7]. A period of rapid acceleration[7], thinning[31], and grounding line retreat[8] then occurred from 2004 to 2011, when melt rates significantly exceeded equilibrium values. A cooler interval beginning in 2012 caused a steadying of the flow[7] and re-advance of the Kohler Glacier grounding line[8], as melting dropped below the now-elevated equilibrium value.

Such behaviour provides insight into the physical processes that link ocean forcing with ice-sheet response. Thermocline shoaling induces thinning of the ice shelf, reducing its contact with margins and seabed, and weakening buttressing at the grounding line[6], where flow accelerates in response[7]. Consequent thinning of inland ice causes retreat of the grounding line[8], further reducing local resistance to flow[32], and steepens the slope of the glacier surface, increasing local forcing of the flow[33]. Those secondary effects induce further acceleration, and develop over time at a rate that is determined by the glacier bed and margin geometries, and the local resistance they provide to the flow[9]. Subsequent deepening of the thermocline reduces melting, causing ice shelf thickening and increased buttressing at the new grounding line. Inland response is now complicated by a continuing adjustment of ice thickness and flow to the earlier perturbation.

The nonlinear relationship between meltwater flux and mean seawater temperature (Fig. 4c) confirms theoretical inferences wherein turbulent ice–ocean heat transfer depends on both the temperature difference across the boundary layer and the shear generated by the far-field geostrophic current, itself driven by temperature-related density differences (Methods). A similar relationship exists in numerical models of sub-ice circulation applied to idealized ice and seabed geometries[34]. That nonlinearity has important implications for ice-shelf vulnerability to changing ocean conditions, enhancing melt rate sensitivity as the mean state temperature rises. For a given temperature increase, ice shelves will thin more rapidly in the warm southeastern Pacific sector than elsewhere on the Antarctic continental shelf, where subsurface seawater temperatures are typically closer to the surface freezing point.

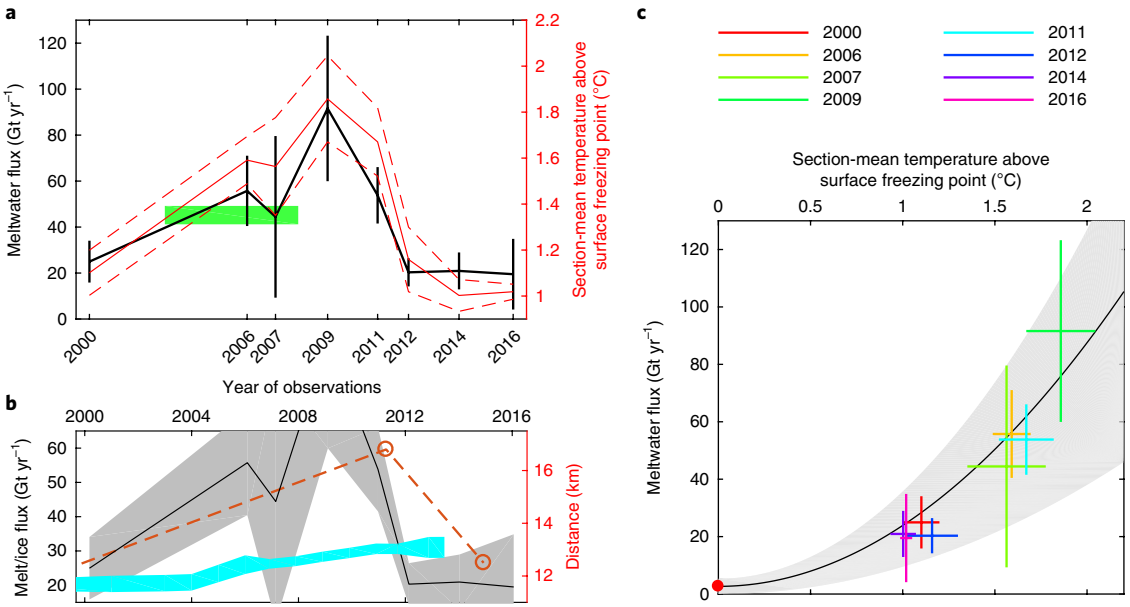

Fig. 4 | Meltwater flux and mean ocean temperature at Dotson Ice Front. a, Time series of meltwater flux (black; error bars represent one standard deviation) and mean temperature above the surface freezing point (red; dashed lines indicate one standard deviation), with melt flux derived from the 2003–2008 satellite data[27] (green bar). **b**, Meltwater flux (black, shading indicates one standard deviation), mass flux across Dotson Ice Shelf grounding line[7] (cyan) and relative position of Kohler Glacier grounding line[8] (red circles linked by dashed line). **c**, Meltwater flux versus mean temperature above the surface freezing point (colour-coded by year, horizontal and vertical error bars are both one standard deviation). The black line is a theoretical quadratic relationship (Methods) with uncertainties (grey shading), using an additional point (red dot) estimated from observations in cold-water sectors of Antarctica[27].

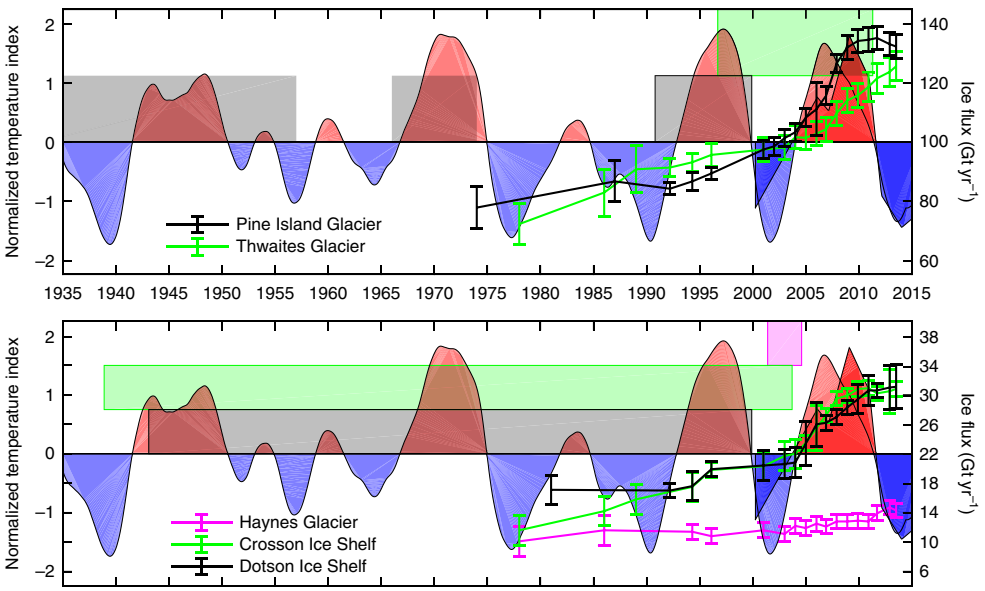

Fig. 5 | Multi-decadal history of ocean forcing and outlet glacier response in the eastern Amundsen Sea. Time series of glacier outflow changes[7] (right-hand axis, with one standard deviation error bars) and ocean forcing (red, warm conditions; blue, cool conditions) as documented here (darker shading) and as inferred (lighter shading) from central tropical Pacific sea surface temperatures[22] (left-hand axis, both normalized). Shaded boxes (outlined and colour-coded by glacier) indicate the range of estimated times for the initiation of the most recent phase of rapid thinning at the grounding lines[9], while boxes without outlines are inferred times of initial and final detachment of Pine Island Glacier from a submarine ridge[15].

Ocean variability as a driver of change in Amundsen Sector

Models and observations give a consistent picture of winds over the continental shelf as the main driver of thermocline depth variability and consequent changes in melting throughout the eastern Amundsen Sea[22,35,36]. Various processes including wind-forced variability of mCDW inflow[37] and near-coastal densification[20,38] and downwelling of Winter Water[39] have been invoked. If critical wind changes are associated with regional circulation anomalies triggered from the tropical Pacific[29,40], forcing during prior decades would have been characterized by similar cycles[22]. Coupled with the nonlinear response of ice-shelf melting, such pronounced variability makes the Amundsen Sea sector of the WAIS particularly susceptible to decadal changes in ice-shelf buttressing.

The region-wide observations of intermittent acceleration[7] and more sustained, but episodic, thinning[9] are explicable in terms of such forcing (Fig. 5). Warm phases are characterized by rapid acceleration in ice flow, as ice shelves thin and buttressing decreases. Flow steadies or decelerates during cool phases, with exceptions because individual glacier bed geometry determines the size of the evolving inland response to the preceding acceleration. The resilience of Kohler Glacier through the recent period of increased melting beneath Dotson Ice Shelf indicates that a grounding line pinned on a prominent seabed rise[8] can limit the response to reduced buttressing and allow recovery during a subsequent cool phase. With a less stable grounding line, acceleration resulting from reduced buttressing can initiate a short period of unstable retreat, triggering an inland-propagating wave of thinning[9], and further acceleration that may override a cooling-induced increase in ice-shelf buttressing. Evidence (Fig. 5) suggests that episodes of retreat occurred in the 1940s, the 1970s and the 1990s on Pine Island Glacier[9,15], in the early 2000s on the Thwaites and Haynes glaciers[9], and with less certain timing on the glaciers feeding Dotson and Crosson ice shelves[9].

Longer-term change may underlie the pronounced decadal variability reported here. That might account for the mean ocean state over the 2000–2016 period being warm enough to induce thinning of Dotson Ice Shelf (Fig. 4b). However, inland thinning of Kohler Glacier[9] indicates a retreat episode prior to 2000 (Fig. 5). Associated deepening of the grounding line would have exposed more of the ice shelf base to the warmer mCDW, elevating the melt rate for equivalent ocean forcing. The absence of significant inland thinning on Pine Island Glacier prior to the 1990s retreat[9] suggests that a near-equilibrium state was re-established there following major perturbations in the 1940s and 1970s[15].

It now appears that recent accelerated mass loss from the Amundsen Sea sector of the WAIS has not resulted from progressive ocean warming or unstable ice retreat, but rather from a combination of analogous processes whereby successive warm intervals trigger episodic retreats of the most vulnerable grounding lines, adding to a longer-term inland response. Over recent decades, pauses in acceleration and minor decelerations in Amundsen Sea outlet glaciers during cool periods (Fig. 5) may have reduced the rate of ice loss from West Antarctica, as documented since 2011 for the current cool phase[41]. Determining the magnitude of committed loss from past and future warm episodes will require a better understanding of what drives the strong temporal variability of the mid-depth thermocline that dominates the recent record of ice-shelf water properties and of how the ice shelves and outlet glaciers respond.

Methods

Methods, including statements of data availability and any associated accession codes and references, are available at https://doi.org/10.1038/s41561-018-0207-4.

Received: 16 April 2018; Accepted: 17 July 2018;
Published online: 13 August 2018

References

1. Shepherd, A. et al. A reconciled estimate of ice-sheet mass balance. *Science* **338**, 1183–1189 (2012).
2. Fretwell, P. et al. Bedmap2: improved ice bed, surface and thickness datasets for Antarctica. *Cryosphere* **7**, 375–393 (2013).
3. Schoof, C. Ice sheet grounding line dynamics: steady states, stability, and hysteresis. *J. Geophys. Res.* **112**, F03S28 (2007).
4. Goldberg, D., Holland, D. M. & Schoof, C. Grounding line movement and ice shelf buttressing in marine ice sheets. *J. Geophys. Res.* **114**, F04026 (2009).
5. Gudmundsson, G. H. Ice-shelf buttressing and the stability of marine ice sheets. *Cryosphere* **7**, 47–655 (2013).
6. Reese, R., Gudmundsson, G. H., Levermann, A. & Winkelmann, R. The far reach of ice-shelf thinning in Antarctica. *Nat. Clim. Change* **8**, 53–57 (2018).
7. Mouginot, J., Rignot, E. & Scheuchl, B. Sustained increase in ice discharge from the Amundsen Sea Embayment, West Antarctica, from 1973 to 2013. *Geophys. Res. Lett.* **41**, 1576–1584 (2014).
8. Scheuchl, B., Mouginot, J., Rignot, E., Morlighem, M. & Khazendar, A. Grounding line retreat of Pope, Smith, and Kohler Glaciers, West Antarctica, measured with Sentinel-1a radar interferometry data. *Geophys. Res. Lett.* **43**, 8572–8579 (2016).
9. Konrad, H. et al. Uneven onset and pace of ice-dynamical imbalance in the Amundsen Sea Embayment, West Antarctica. *Geophys. Res. Lett.* **44**, 910–918 (2017).
10. Thomas, R. H., Sanderson, T. J. O. & Rose, K. E. Effect of climatic warming on the West Antarctic ice sheet. *Nature* **277**, 355–358 (1979).
11. Jacobs, S. S., Hellmer, H. H. & Jenkins, A. Antarctic ice sheet melting in the southeast Pacific. *Geophys. Res. Lett.* **23**, 957–960 (1996).
12. Paolo, F. S., Fricker, H. A. & Padman, L. Volume loss from Antarctic ice shelves is accelerating. *Science* **348**, 327–331 (2015).
13. Favier, L. et al. Retreat of Pine Island Glacier controlled by marine ice-sheet instability. *Nat. Clim. Change* **4**, 117–121 (2014).
14. Joughin, I., Smith, B. E. & Medley, B. Marine ice sheet collapse potentially under way for the Thwaites Glacier basin, West Antarctica. *Science* **344**, 735–738 (2014).
15. Smith, J. A. et al. Sub-ice shelf sediments record 20th century retreat history of Pine Island Glacier. *Nature* **541**, 77–80 (2017).
16. Hillenbrand, C.-D. et al. West Antarctic Ice Sheet retreat driven by Holocene warm water incursions. *Nature* **547**, 43–48 (2017).
17. Schmidtko, S., Heywood, K. J., Thompson, A. F. & Aoki, S. Multidecadal warming of Antarctic waters. *Science* **346**, 1227–1231 (2014).
18. Jacobs, S. S., Jenkins, A., Giulivi, C. F. & Dutrieux, P. Stronger ocean circulation and increased melting under Pine Island Glacier ice shelf. *Nat. Geosci.* **4**, 519–523 (2011).
19. Dutrieux, P. et al. Strong sensitivity of Pine Island ice-shelf melting to climatic variability. *Science* **343**, 174–178 (2014).
20. Webber, B. G. M. et al. Mechanisms driving variability in the ocean forcing of Pine Island Glacier. *Nat. Commun.* **7**, 14507 (2017).
21. Christianson, K. et al. Sensitivity of Pine Island Glacier to observed ocean forcing. *Geophys. Res. Lett.* **43**, 10817–10825 (2016).
22. Jenkins, A. et al. Decadal ocean forcing and Antarctic Ice Sheet response: lessons from the Amundsen Sea. *Oceanography* **29**, 106–117 (2016).
23. Jacobs, S. et al. Getz Ice Shelf melting response to changes in ocean forcing. *J. Geophys. Res. Oceans* **118**, 4152–4168 (2013).
24. Jacobs, S. et al. The Amundsen Sea and the Antarctic Ice Sheet. *Oceanography* **25**, 154–163 (2012).
25. Wåhlin, A. K., Yuan, X., Björk, G. & Nohr, C. Inflow of warm Circumpolar Deep Water in the central Amundsen shelf. *J. Phys. Oceanogr.* **40**, 1427–1434 (2010).
26. Ha, H. K. et al. Circulation and Modification of Warm Deep Water on the central Amundsen shelf. *J. Phys. Oceanogr.* **44**, 1493–1501 (2014).
27. Rignot, E., Jacobs, S., Mouginot, J. & Scheuchl, B. Ice-shelf melting around Antarctica. *Science* **341**, 266–270 (2013).
28. Gourmelen, N. et al. Channelized melting drives thinning under a rapidly melting Antarctic ice shelf. *Geophys. Res. Lett.* **44**, 9796–9804 (2017).
29. Paolo, F. S. et al. Response of Pacific-sector Antarctic ice shelves to the El Niño/Southern Oscillation. *Nat. Geosci.* **11**, 121–126 (2018).
30. Lilien, D. A., Joughin, I., Smith, B. & Shean, D. E. Changes in flow of Crosson and Dotson ice shelves, West Antarctica, in response to elevated melt. *Cryosphere* **12**, 1415–1431 (2018).
31. Khazendar, A. et al. Rapid submarine ice melting in the grounding zones of ice shelves in West Antarctica. *Nat. Commun.* **7**, 13243 (2016).
32. Payne, A. J., Vieli, A., Shepherd, A. P., Wingham, D. J. & Rignot, E. Recent dramatic thinning of largest West Antarctic ice stream triggered by oceans. *Geophys. Res. Lett.* **31**, L23401 (2004).
33. Scott, J. B. T. et al. Increased rate of acceleration on Pine Island Glacier strongly coupled to changes in gravitational driving stress. *Cryosphere* **3**, 125–131 (2009).
34. Holland, P. R., Jenkins, A. & Holland, D. M. The response of ice shelf basal melting to variations in ocean temperature. *J. Climate* **21**, 2558–2572 (2008).
35. Kimura, S. et al. Oceanographic controls on the variability of ice-shelf basal melting and circulation of glacial meltwater in the Amundsen Sea Embayment, Antarctica. *J. Geophys. Res. Oceans* **122**, 10131–10155 (2017).
36. Turner, J. et al. Atmosphere-ocean-ice interactions in the Amundsen Sea Embayment, West Antarctica. *Rev. Geophys.* **55**, 235–276 (2017).
37. Thoma, M., Jenkins, A., Holland, D. & Jacobs, S. Modelling Circumpolar Deep Water intrusions on the Amundsen Sea continental shelf, Antarctica. *Geophys. Res. Lett.* **35**, L18602 (2008).
38. St-Laurent, P., Klinck, J. M. & Dinniman, M. S. Impact of local winter cooling on the melt of Pine Island Glacier, Antarctica. *J. Geophys. Res. Oceans* **120**, 6718–6732 (2015).

39. Kim, C. S. et al. Is Ekman pumping responsible for the seasonal variation of warm circumpolar deep water in the Amundsen Sea? *Cont. Shelf Res.* **132**, 38–48 (2017).
40. Steig, E. J., Ding, Q., Battisti, D. S. & Jenkins, A. Tropical forcing of Circumpolar Deep Water inflow and outlet glacier thinning in the Amundsen Sea Embayment, West Antarctica. *Ann. Glaciol.* **53**, 19–28 (2012).
41. The IMBIE Team. Mass balance of the Antarctic Ice Sheet from 1992 to 2017. *Nature* **558**, 219–222 (2018).

Acknowledgements

We are grateful to all cruise participants who assisted in the collection of the data. A.J. and D.S. were supported by core funding from the UK Natural Environment Research Council (NERC) to the British Antarctic Survey's Polar Oceans Program. P.D. was supported by funding from NERC's iSTAR Programme through grant NE/J005770/11 and NSF grant 1643285. S.J.'s support included NSF grants ANT06-32282 and 16-44159. Support for S.H.L. and T.W.K. was provided by the Korea Polar Research Institute grant KOPRI PE17060. S.S. was supported by National Science Foundation Office of Polar Programs collaborative grants 0838975 and 1443569.

Author contributions

A.J., D.S., P.D. and S.J. conceived the study. D.S., S.J., T.W.K., S.H.L., H.K.H. and S.S. planned and led the data collection. D.S., P.D. and T.W.K. processed the data. A.J., D.S. and P.D. undertook the data analyses and derivation of the final results. A.J. prepared the manuscript. All authors discussed the results and implications and commented on the manuscript at all stages.

Competing interests

The authors declare no competing interests.

Additional information

Supplementary information is available for this paper at https://doi.org/10.1038/s41561-018-0207-4.

Reprints and permissions information is available at www.nature.com/reprints.

Correspondence and requests for materials should be addressed to A.J.

Publisher's note: Springer Nature remains neutral with regard to jurisdictional claims in published maps and institutional affiliations.

Methods

Data collection. Data were collected from three marine research vessels during eight summer visits to the Amundsen Sea (Supplementary Table 1). All cruises used Sea-Bird Scientific SBE 911plus conductivity–temperature–depth (CTD) profiling systems, with consistent recording and processing procedures. On seven cruises, dissolved oxygen sensors were added to the system, and on five cruises, lowered acoustic Doppler current profilers were mounted on the CTD frame. Scalar data were averaged into 1- or 2-dbar pressure bins, while current data were averaged into larger bins, typically of 20 dbar. Most section profiles were regularly spaced within a few hundred metres of the Dotson Ice Front (Fig. 1 and Supplementary Fig. 1).

Meltwater fraction calculations. As ice melts into seawater the resulting water mass becomes cooler, fresher and richer in dissolved oxygen than the original water. Most of the cooling occurs because the seawater supplies the latent heat required for the phase change, freshening because of the addition of meltwater, and dissolved oxygen concentrations rise as air bubbles trapped in the ice go into solution. Any combination of potential temperature, salinity and dissolved oxygen can be used to diagnose the meltwater content as the third component of a mixture incorporating mCDW and Winter Water as the other end-members[42] (Supplementary Table 2). Ice properties are assumed to be constant, whereas mCDW and Winter Water properties are cruise-specific and are defined by reference to the distribution of data in property–property plots (Supplementary Fig. 2).

In property–property space, the data lie within a triangle defined by straight lines originating from the mCDW properties[42]. One line connects the mCDW and ice end-points and indicates seawater properties that arise from ice melting into 'pure' mCDW. A second line connecting mCDW and Winter Water end-points represents properties that arise from mixing between the 'pure' Winter Water and mCDW. Mixtures on the second line contain no meltwater and define the 'ambient' water column that interacts with the ice. The distance that a point lies from the 'ambient' line indicates the meltwater content that can be quantified as[42]:

$$\phi = \frac{(\chi^2 - \chi^2_{\mathrm{mCDW}}) - (\chi^1 - \chi^1_{\mathrm{mCDW}})(\chi^2_{\mathrm{WW}} - \chi^2_{\mathrm{mCDW}})/(\chi^1_{\mathrm{WW}} - \chi^1_{\mathrm{mCDW}})}{(\chi^2_{\mathrm{ICE}} - \chi^2_{\mathrm{mCDW}}) - (\chi^1_{\mathrm{ICE}} - \chi^1_{\mathrm{mCDW}})(\chi^2_{\mathrm{WW}} - \chi^2_{\mathrm{mCDW}})/(\chi^1_{\mathrm{WW}} - \chi^1_{\mathrm{mCDW}})}$$

where φ is the meltwater fraction, χ^i represents potential temperature, salinity or dissolved oxygen, and subscripts indicate defined water mass properties (Supplementary Table 2).

Winter Water is formed when heat loss to the atmosphere causes freezing at the sea surface. As the sea ice grows, salt is rejected from the solid phase, increasing surface water salinity and driving convection. The result is a deep mixed layer with a temperature at the surface freezing point and a salinity that varies from year to year, depending on the amount and salinity of sea ice grown during the winter. Formed by air–sea interaction at the surface, Winter Water is rich in dissolved oxygen, but not necessarily saturated because the consolidating ice cover presents a barrier to air–sea gas exchange. Since 'pure' Winter Water, having a temperature at the surface freezing point, is absent from the summertime ice-front sections, we estimate a range of possible properties (Supplementary Table 2, Supplementary Fig. 2) and investigate the sensitivity of results to that property range. The mCDW properties are defined as the intersection between the ice/mCDW mixing line, which connects the ice properties with one edge of the data 'triangle', and the Winter Water/mCDW mixing line, which connects the mid-range of the Winter Water properties with the other edge of the data 'triangle' (Supplementary Fig. 2).

In some of the cold years we find that the mCDW properties thus defined do not correspond to the warmest waters near the ice front, indicating a lack of direct interaction with the ice. This points to recirculation deeper than the ice shelf draught, or exclusion from the inner cavity by a seabed shoal[43], as on Pine Island Glacier[44,45]. Heat from those waters could still contribute to melting if mixed into the thermocline. In other years the mCDW properties are warmer and saltier than any waters near the ice front, an indication that some seawater arriving at the ice front has formed from ice melting into the warmer and saltier mCDW in Pine Island Bay[24]. Those waters flow westward along the continental shelf[45,46] and carry meltwater beneath Dotson Ice Shelf.

Profiles of meltwater fraction, calculated using mid-range Winter Water properties, are shown for all stations in Supplementary Fig. 3. Since interaction with the atmosphere can influence all three tracers, the assumption of a mixture of three water masses breaks down near the sea surface. In principle, a fourth water mass of surface water could be defined, but in practice the surface properties are too spatially heterogeneous to be defined as a single water mass. Instead we use the scatter of results derived from the three separate calculations of meltwater fraction to indicate where atmospheric interaction (or another process) makes the results unreliable (Supplementary Fig. 3). This exclusion will lower net melting estimates if cavity outflows are light enough to upwell into the surface layer. Sections of potential temperature, salinity and dissolved oxygen are shown in Supplementary Fig. 1 and derived meltwater fractions are shown in Supplementary Fig. 3.

Meltwater transport calculations. The net flux of meltwater away from the ice shelf is calculated by combining estimates of meltwater fraction and currents perpendicular to the ice front. While the latter can be observed directly, as during some cruises (Supplementary Table 1), inherently large measurement uncertainties are compounded by high-frequency variability associated with tides, waves and eddies that contaminate the longer-term mean flow relevant to the calculation of meltwater transport. However, higher-frequency processes have a smaller impact on the density structure derived from measurements of temperature and salinity, which is of greater value in estimating the longer-term mean circulation[47].

At spatial scales larger than the local internal Rossby radius (a few kilometres) the pressure gradient that drives the flow is balanced primarily by the Coriolis force it generates, allowing across-section currents to be estimated from along-section pressure gradients. To make direct use of the pressure recorded by the CTD, it is convenient to work in an isobaric framework, in which the geostrophic currents can be derived from the slope of isobars relative to geopotential surfaces. Because isobar depth is the integral of specific volume (reciprocal of density) from the surface down to the relevant pressure, the relative isobar slope between any two stations can readily be derived from the CTD data. The absolute isobar slope remains unknown because the slope of the sea surface relative to the geoid cannot be precisely measured, introducing a pressure-independent unknown into the calculated isobaric slopes. Calculated currents thus include a CTD-derived, pressure-dependent component, and a pressure-independent component that must be estimated in some other way:

$$v(P) = v(P_{\mathrm{ref}}) + \frac{1}{f}\frac{\partial}{\partial x}\left(\int_P^{P_{\mathrm{ref}}} \alpha \mathrm{d}P\right)\Bigg|_P$$

where x is the along-section coordinate, v is the across-section current, P is pressure, α is specific volume, f is the Coriolis parameter, and P_{ref} refers to an arbitrary reference pressure where the flow associated with the absolute slope of the isobar must be determined[47].

The conventional solution is then to select a pressure level at which it is physically reasonable to assume that the isobar is parallel to the geoid and hence that the velocity is zero. For the Dotson Ice Front sections, such a level of zero motion might be the maximum depth on each station at which meltwater is found (Supplementary Fig. 3). Zero motion at that level would be consistent with a pure overturning circulation with warm inflow at depth and outflows of glacially modified water at shallower levels. Given the large scale of the ocean cavity beneath Dotson Ice Shelf compared with the internal Rossby radius, we should anticipate a significant horizontal, geostrophic circulation accompanying the overturning[18,19]. The magnitude of the horizontal circulation can be estimated by adapting a procedure for inferring reference-level currents[48]. Since the CTD sections completely enclose a volume of the ocean, integral constraints on the circulation across the section can be derived from the conservation of mass and scalar properties, along with a steady-state assumption within that volume. Flow between individual station pairs can then be adjusted by adding to each a non-zero $v(P_{\mathrm{ref}})$ that makes the overall circulation compatible with the constraints. With typically fewer constraints than unknown reference velocities, yielding infinitely many solutions that satisfy the constraints exactly, the adopted strategy is to choose the solution that minimizes the sum of the squares of the reference velocities (the solution that is closest, in terms of the L_2 norm, to the original circulation with zero reference velocities).

The next problem is that the conventional approach of imposing zero mass, heat and salt fluxes at the ice front constrains the solution to give a net meltwater flux of zero across the section, in turn requiring a novel strategy to overcome that limitation[47]. Knowing the ice properties (Supplementary Table 2), the impact of meltwater addition on all conservation equations (mass, heat, salt and dissolved oxygen, where measured) can be quantified in terms of the yet-to-be-determined meltwater flux. The mass conservation equation can then be used to eliminate the unknown melt rate from the other equations. The system yields as many constraints as there are tracers observed, effectively balancing the budgets associated with the circulation of meltwater-free source waters, and the resulting imbalance between total inflow and outflow is the sought-after meltwater flux (Supplementary Table 3). Another estimate of the meltwater flux can be obtained from the net transport of meltwater fraction, quantified as described above, associated with the derived circulation. Both estimates yield the net meltwater flux across the section, with the latter additionally giving the meltwater concentration in the inflow that is sourced from elsewhere (Supplementary Table 3) and the total in the outflow. The two estimates of the melt added from the ice shelf are independent, since the first requires only that integrated inflow and integrated outflow properties be connected by a meltwater mixing line. It is thus formally independent of the choice of Winter Water and mCDW properties, although indirect use is made of the scatter in meltwater fraction calculations to determine how much of the water column to exclude from the budget calculations. The scatter indicates where air–sea exchange exerts an influence on water properties (Supplementary Fig. 3), and that part of the upper water column is excluded from budget calculations that assume that the only changes between inflow and outflow result from meltwater addition.

The initial circulation, adjustments and final circulation derived using mid-range Winter Water properties are shown for each section in Supplementary Fig. 4,

with analogous results from available directly observed currents in Supplementary Fig. 5. As the largest currents associated with the undesired high-frequency variability are likely to be approximately pressure-independent, an identical technique preserves the observed depth-dependent current structure, but closes budgets by adding depth-independent velocity adjustments calculated as described above. Prior de-tiding of the observed currents has a negligible impact on the results, because tidal currents near Dotson Ice Shelf are typically much smaller than the applied adjustments.

Since some underlying assumptions, particularly that of steady, geostrophic flow, will hold only approximately, any one solution will generally provide an unreliable estimate of the circulation and ice-shelf melt rate. Indeed, applying all constraints can sometimes yield excessively noisy solutions, since we are forcing inherently noisy observations to fit our assumptions exactly. We therefore generate the inverse of the constraint matrix using a singular value decomposition, and we use a truncated rather than a full-rank solution if the latter is excessively noisy[48]. With at most three constraints, this amounts to a choice between three (full-rank) or two (truncated) singular vectors. The procedure is repeated for all realizations of the Winter Water properties (Supplementary Table 2), and each solution is scored on the basis of three measures of solution credibility:

$$\mathrm{Score}=\frac{1}{3}\left\{\left(1-\min\left[1,\frac{v_{\mathrm{rms}}^{\mathrm{adj}}}{V_{\mathrm{rms}}^{\mathrm{adj}}}\right]\right)+\left(1-\min\left[1,\frac{v_{\mathrm{max}}^{\mathrm{adj}}}{V_{\mathrm{max}}^{\mathrm{adj}}}\right]\right)+\left(1-\min\left[1,\frac{\delta m}{\Delta M}\right]\right)\right\}$$

where the three criteria are the root-mean-square velocity adjustment, $v_{\mathrm{rms}}^{\mathrm{adj}}$; the maximum absolute adjustment, $v_{\mathrm{max}}^{\mathrm{adj}}$; the difference between the transport imbalance and the net flux of meltwater fraction across the section, δm. In each case we specify a tolerance beyond which the solution scores 0 for that criterion:

$$V_{\mathrm{rms}}^{\mathrm{adj}}=0.1\ \ \mathrm{m\ \ s^{-1}};\ V_{\mathrm{max}}^{\mathrm{adj}}=0.2\ \ \mathrm{m\ \ s^{-1}};\ \Delta M=20\ \ \mathrm{Gt\ \ yr^{-1}}$$

with levels chosen to remove the influence of the majority of physically unreasonable solutions. Additionally, the score for any solution with a meltwater flux less than zero or a circulation greater than 2 Sv is set to zero regardless of the other criteria. All solutions are shown in Supplementary Fig. 6, along with the score-weighted mean and score-weighted standard deviation that provide the final results plotted in Fig. 4. Further results are summarized in Supplementary Table 3.

Theoretical relationship between meltwater flux and ocean temperature. Melting at the base of an ice shelf cools and freshens the water near the ice base and creates a buoyant current that flows along the ice–ocean interface. The melt rate (m) is determined by the heat flux across the turbulent boundary layer created by current shear against the ice base, and can be quantified as[49]:

$$m=\left\{\frac{C_{\mathrm{d}}^{1/2}\Gamma_{\mathrm{TS}}}{(L_i-c_iT_{*i})\ /\ c}\right\}UT_*$$

where U is current speed, $T_*=T-T_{\mathrm{f}}$ is temperature relative to the salinity-dependent freezing point at the depth of the ice shelf base, sometimes referred to as thermal driving, c is the specific heat capacity, L is the latent heat of fusion, C_{d} is the drag coefficient, Γ_{TS} is a heat exchange coefficient, and the subscript 'i' indicates ice properties. If the drag and thermal exchange coefficients are assumed to be constant, the term in braces, which we denote M_0, is approximately constant, as it depends only weakly on the ice temperature relative to the seawater freezing point.

Assuming the large-scale circulation to be in geostrophic balance, the speed of the buoyant boundary current relative to the lower layer of inflowing water, $\Delta U=U-U_{\mathrm{in}}$, can be written[50]:

$$\Delta U=\frac{g}{f}\sin\theta\Delta\rho$$

where g is gravity, f is the Coriolis parameter, Θ is the slope of the ice shelf base relative to the horizontal and $\Delta\rho=(\rho-\rho_{\mathrm{in}})/\rho_{\mathrm{in}}$, the dimensionless density deficit in the boundary current. The transports in the lower, inflowing layer and the buoyant boundary current are approximately equal, differing only because of the addition of meltwater to the latter, so if both layers are of similar thickness, the speed of the buoyant current can be approximated as:

$$U\approx\frac{\Delta U}{2}$$

The properties of the boundary current must lie somewhere along the mixing line connecting the properties of the inflow with those of the ice (the green lines in Supplementary Fig. 2), so the temperature and salinity differences are related by[42]:

$$\frac{(T-T_{\mathrm{in}})}{(S-S_{\mathrm{in}})}=\frac{T_{*\mathrm{in}}+(L_i-c_iT_{*i})\ /\ c}{S_{\mathrm{in}}}$$

Combining this expression with a linear equation of state:

$$\Delta\rho=\beta_S(S-S_{\mathrm{in}})-\beta_T(T-T_{\mathrm{in}})$$

and a linear equation for the freezing point at the depth of the ice shelf base as a function of salinity:

$$(T_*-T_{*\mathrm{in}})=(T-T_{\mathrm{in}})-\lambda_1(S-S_{\mathrm{in}})$$

leads to an expression for the density deficit in terms of the thermal driving deficit[50]:

$$\Delta\rho=(T_*-T_{*\mathrm{in}})\left\{\frac{\beta_SS_{\mathrm{in}}-\beta_T[T_{*\mathrm{in}}+(L_i-c_iT_{*i})\ /\ c]}{T_{*\mathrm{in}}+(L_i-c_iT_{*i})/c-\lambda_1S_{\mathrm{in}}}\right\}$$

Once again the term in braces, which we denote P_0, is approximately constant because of the weak dependence on the ice and inflow temperatures and the small range in inflow salinity.

Thermal driving in the boundary current must be less than that in the inflow, but greater than zero (if the ice shelf base is melting), a condition that can be expressed as:

$$T_*=\varepsilon T_{*in};\ \ 0<\varepsilon<1$$

and combining all the above results leads to an expression for the melt rate that is a quadratic function of the inflow temperature:

$$m=M_0\frac{g}{2f}\sin\theta P_0\varepsilon(\varepsilon-1)T_{*\mathrm{in}}^2$$

The term ε can be related to the relative efficiency of mixing across the thermocline that separates the boundary current from the warmer water below and across the ice–ocean boundary layer. One way to estimate the magnitude of ε is to assume an approximate balance between the vertical turbulent heat fluxes that act to warm and cool, respectively, the boundary current[34,49,51]. The former is often parameterized as a process of entrainment into the boundary current, whereby the entrainment rate is expressed as a function of the current speed and the boundary slope, while the latter is simply the heat flux that drives melting, defined above:

$$E_0\Delta U\sin\theta\,(T_{*\mathrm{in}}-T_*)\approx C_{\mathrm{d}}^{1/2}\Gamma_{\mathrm{TS}}UT_*$$

Both heat fluxes scale with the speed of the boundary current, in recognition of the fact that current shear drives the turbulent mixing. Using the above balance, the expression for ε becomes:

$$\varepsilon\approx\frac{2E_0\sin\theta}{C_{\mathrm{d}}^{1/2}\Gamma_{\mathrm{TS}}+2E_0\sin\theta}$$

The neglect of heat advection within the boundary current in formulating the above balance of vertical turbulent fluxes is inappropriate when the inflow temperature is close to the surface freezing point and advection becomes critical in creating regions of basal freezing (where ε becomes negative). A pragmatic solution is to evaluate the thermal driving in the above theory relative to the surface freezing point and to define an offset at zero thermal driving, where the theory would give a melt rate of zero, from observations on ice shelves in cold oceanic environments, where a spatial average over regions of basal melting and freezing typically gives a small net melt rate[27].

Taking conventional values for physical constants ($g=9.8\,\mathrm{m\,s^{-2}}$, $f=-1.4\times10^{-4}\,\mathrm{s^{-1}}$, $L_i=3.4\times10^5\,\mathrm{J\,kg^{-1}}$, $c_i=2.0\times10^3\,\mathrm{J\,kg^{-1}\,K^{-1}}$, $c=4.0\times10^3\,\mathrm{J\,kg^{-1}\,K^{-1}}$, $\beta_S=7.9\times10^{-4}$, $\beta_T=3.9\times10^{-5}\,\mathrm{K^{-1}}$, $\lambda_1=-5.7\times10^{-2}\,\mathrm{K}$) and parameters ($E_0=3.6\times10^{-2}$, $C_{\mathrm{d}}^{1/2}\Gamma_{\mathrm{TS}}=5.9\times10^{-4}$), choosing appropriate mean values for Dotson Ice Shelf ($S_{\mathrm{in}}=34.5$, $T_{\mathrm{i}}=-15\,^{\circ}\mathrm{C}$, $\sin\Theta=8\times10^{-3}$), and defining a zero thermal driving offset of 0.5 m yr^{-1}, yields the curve plotted in Fig. 4c. The shading around that line indicates the range of curves obtained when the parameters and input data for Dotson Ice Shelf are individually varied by ±50% (but ±10% in the case of S_{in}, because known variations are small, and ±100% for the zero thermal driving offset).

Data availability. The oceanographic data that support the findings of this study are available from the US Antarctic Program Data Center (USAP-DC, http://www.usap-dc.org/), a member of the Interdisciplinary Earth Data Alliance (IEDA), with the identifier https://doi.org/10.15784/601105. Raw and processed data for individual cruises, along with details of the processing, can also be obtained upon reasonable request from the points of contact listed in Supplementary Table 1.

Code availability. The Matlab scripts used for the analyses described in this study, along with data files formatted for use with the software, can be obtained from the corresponding author upon reasonable request.

References

42. Jenkins, A. The impact of melting ice on ocean waters. *J. Phys. Oceanogr.* **29**, 2370–2381 (1999).
43. Millan, R., Rignot, E., Bernier, V., Morlighem, M. & Dutrieux, P. Bathymetry of the Amundsen Sea Embayment sector of West Antarctica from Operation IceBridge gravity and other data. *Geophys. Res. Lett.* **44**, 1360–1368 (2017).
44. Jenkins, A. et al. Observations beneath Pine Island Glacier in West Antarctica and implications for its retreat. *Nat. Geosci.* **3**, 468–472 (2010).
45. Biddle, L. C., Heywood, K. J., Kaiser, J. & Jenkins, A. Glacial meltwater identification in the Amundsen Sea. *J. Phys. Oceanogr.* **47**, 933–954 (2017).
46. Nakayama, Y., Schröder, M. & Hellmer, H. H. From Circumpolar Deep Water to the glacial meltwater plume on the eastern Amundsen Shelf. *Deep-Sea Res. I* **77**, 50–62 (2013).
47. Jenkins, A. & Jacobs, S. S. Circulation and melting beneath George VI Ice Shelf, Antarctica. *J. Geophys. Res.* **113**, C04013 (2008).
48. Wunsch, C. The North Atlantic general circulation west of 50°W determined by inverse methods. *Rev. Geophys. Space Phys.* **16**, 583–620 (1978).
49. Jenkins, A. Convection-driven melting near the grounding lines of ice shelves and tidewater glaciers. *J. Phys. Oceanogr.* **41**, 2279–2294 (2011).
50. Jenkins, A. A simple model of the ice shelf–ocean boundary layer and current. *J. Phys. Oceanogr.* **46**, 1785–1803 (2016).
51. Little, C. M., Gnanadesikan, A. & Oppenheimer, M. How ice shelf morphology controls basal melting. *J. Geophys. Res.* **114**, C12007 (2009).